Title

Preparation of damage-free kerogen specimen for microscopy: Understanding the damage mechanisms induced by ion milling techniques

Authors

Xie, Yujun

Huang, Xi

Aldajani, Saleem

et al.

Publication Date

2024-03-01

DOI

10.1016/j.geoen.2023.212607

234 (2024) 212607

Contents lists available at ScienceDirect

Geoenergy Science and Engineering

journal homepage: www.sciencedirect.com/journal/geoenergy-science-and-engineering

Preparation of damage-free kerogen specimen for microscopy: Understanding the damage mechanisms induced by ion milling techniques

Yujun Xie [a,b], Xi Huang [b], Saleem Aldajani [b], Hi T. Vo [b], Danielle M. Jorgens [c], Younane Abousleiman [d], Katherine Hull [e,*], Peter Hosemann [b,f,**]

[a] Global Institute of Future Technology, Shanghai Jiao Tong University, Shanghai, 200240, China
[b] Department of Nuclear Engineering, University of California at Berkeley, Berkeley, CA, 94720, USA
[c] Electron Microscope Laboratory, University of California at Berkeley, Berkeley, CA, 94720 USA
[d] School of Geosciences, Integrated PoroMechanics Institute, The University of Oklahoma, Norman, OK, USA
[e] Aramco Research Center—Houston, Aramco Services Company, 16300 Park Row, Houston, TX, 77084, USA
[f] Materials Science Division, Lawrence Berkeley National Laboratory, Berkeley, CA, 94720, USA

ARTICLE INFO

Keywords:
Kerogen
Shale
Focused ion beam
Cryomicrotome
Beam damage

ABSTRACT

Focused ion beam (FIB) milling techniques have been used for more than a decade to prepare organic-rich shale samples for electron microscopy. Nano- and micro-scale imaging of organic pores is used to assess pore volumes and hence estimate gas-in-place. Ion milling natural composites is particularly challenging due to drastic extremes in the physical properties of individual phases such as minerals and organics. Damage to the organic-rich phases occurs due to the large differences in thermal conductivities of minerals and organics that could reach an order of magnitude and the resulting buildup of heat in the organics. Furthermore, radiation damage via ion implantation may also alter the structural characteristics of the shale.

Herein, the damage associated with preparing electron-transparent kerogen specimen using low kV FIB, cryo-FIB, and cryomicrotome, a new technique for shale kerogen, is quantified using experimental and modeling techniques. The degree of gallium implantation is quantified using scanning transmission electron microscopy (STEM), selected area electron diffraction (SAED), and energy dispersive X-ray spectroscopy (EDX) along with the stopping range of ions in matter (SRIM) model. Interestingly, although the use of cryogenic temperature removes the thermal effect, Ga^{+} ion implantation is observed in the specimen prepared by cryo-FIB.

Furthermore, the magnitude of the thermal damage at a highly localized level was determined using nano-beam electron diffraction (NBED) performed at −196 °C. Time-resolved diffraction patterns indicate that despite the fact kerogen is among the most stable geopolymers, the aromatic components still degraded due to the local temperature increases. On the other hand, the cryomicrotome technique operating at liquid nitrogen temperature is demonstrated as a suitable method to prepare thin kerogen specimen while minimizing structural damage and preserving its native porosity and chemical composition.

1. Introduction

Kerogen in source-rock reservoirs is geological organic matter (OM) with a cross-linked polymeric molecular structure and is a source of petroleum (Sanei, 2020). It is interwoven with the fine-grained clay and non-clay mineral matrix, rendering the composite material challenging for classical (ASTM) rock mechanical characterization (Abousleiman et al., 2016; Hull and Abousleiman, 2016). In addition to burial history and adjacent rock lithology (Inan et al., 2017) among other factors, hydrocarbon reserve estimation in unconventional source rock is dependent upon the porosity, connectivity, and percent volume of OM in the rock (Loucks et al., 2009). Economical production of hydrocarbons from these source rock reservoirs requires hydraulic fracturing stimulation in order to create conductive channels for the gas and condensate to flow into the well (Turcotte et al., 2014). The success of hydraulic fracturing operations relies upon understanding the distribution and maturity of the OM as its pore volume is occupied by the hydrocarbons (Loucks et al., 2009). The chemical composition, pore structure and

* Corresponding author.
** Corresponding author.
E-mail addresses: katherine.hull@aramcoamericas.com (K. Hull), peterh@berkeley.edu (P. Hosemann).

https://doi.org/10.1016/j.geoen.2023.212607
Received 22 May 2023; Received in revised form 13 October 2023; Accepted 22 December 2023
Available online 1 January 2024

connectivity, surface characteristics, and maturity dictate the success of well placement, the hydraulic fracture extension and the fracturing stages in the reservoir (Turcotte et al., 2014). These parameters are necessary for an optimal and economical stimulated reservoir volume (SRV) (Maxwell, 2011).

In order to understand the effects of kerogen on the chemo-mechanical properties of source rocks and upon unconventional reservoir stimulation, well completion and well production, multiscale property characterization and upscaling continues to be of value (Josh et al., 2012). To that end, and early on, nanoindentation was used to characterize source rocks with their in-situ kerogen mechanical properties and their clay minerals anisotropic stiffness values (Bennett et al., 2015; Ulm and Abousleiman, 2006; Zeszotarski et al., 2004). These nano-/micro-scale characterization methods were used to study micro-sized kerogen-rich source rock specimen, such as micro-cantilever beams and pillars and were tested for their composite behavior in tension and compression (Abousleiman et al., 2016; Hull et al., 2017; Zhao and Zhang, 2020). However, undesired damage during sample preparation was clearly noticeable, when extended use of the focused ion beam (FIB) could alter the kerogen's organic matrix, and its pore structure, thereby altering its mechanical, physical, and chemical properties. Heat, sputtering, and ion deposition could easily be observed to affect the organic phase porosities though kerogen is the most stable geopolymer. Previous studies featured ion beam damage in metals and ceramics during sample preparation (Babu et al., 2016; Kiener et al., 2007). FIB milling has the potential to raise the near-surface temperature of low thermal conductivity (<1 W. $m^{-1}.K^{-1}$) materials causing thermal damage in soft materials (Mayer et al., 2007; Orthacker et al., 2014; Schmied et al., 2014; Volkert and Minor, 2007). Kerogen as a crosslinked polymer has a low thermal conductivity relative to the surrounding minerals, (Rajeshwar et al., 1980) rendering it difficult to isolate from damage when ion milling at high exposure times in order to mill the hard minerals (Fig. 1). Degradation of the OM, particularly in samples with lower thermal maturities (i.e., lower thermal conductivity) will affect image-based physical interpretations and can lead to inaccurate porosity and permeability upscaling, and hence erroneous reservoir storativity, and volumes of hydrocarbon's reservoir capacity (Katz and Arango, 2018; Milner et al., 2010; Sanei and Ardakani, 2016).

Despite the highly sensitive nature of the polymeric structure of kerogen to ion milling, none of the studies thoroughly account for the effect of the unavoidable ion beam damage during the image-based interpretation of kerogen's physical properties such as porosity. Previous work proposed that transfer of kinetic energy to heat from low-energy broad ion beam (BIB) milling causes thermal alteration of sedimentary OM, resulting in increases of OM reflectance (Sanei and Ardakani, 2016) though further spectroscopic investigation demonstrated minimal thermal alteration from BIB (Hackley et al., 2020). The OM reflectance increase from BIB milling may instead be due to decreased surface roughness (Grobe et al., 2017; Valentine et al., 2019). Significant Ga^{+} ion implantation is also reported in the chemical analysis of soil specimen prepared by cryo-FIB and whether implantation in kerogen could have any effect remains unknown (Possinger et al., 2020). Hence, different strategies are needed to validate the preparation of electron transparent kerogen specimen with pristine structure, which simultaneously requires in-depth understanding of the ion milling damage mechanism with advanced characterization techniques. Though numerous techniques continue to be developed for understanding the thermal alteration of OM including Raman spectroscopy (Ferralis et al.,

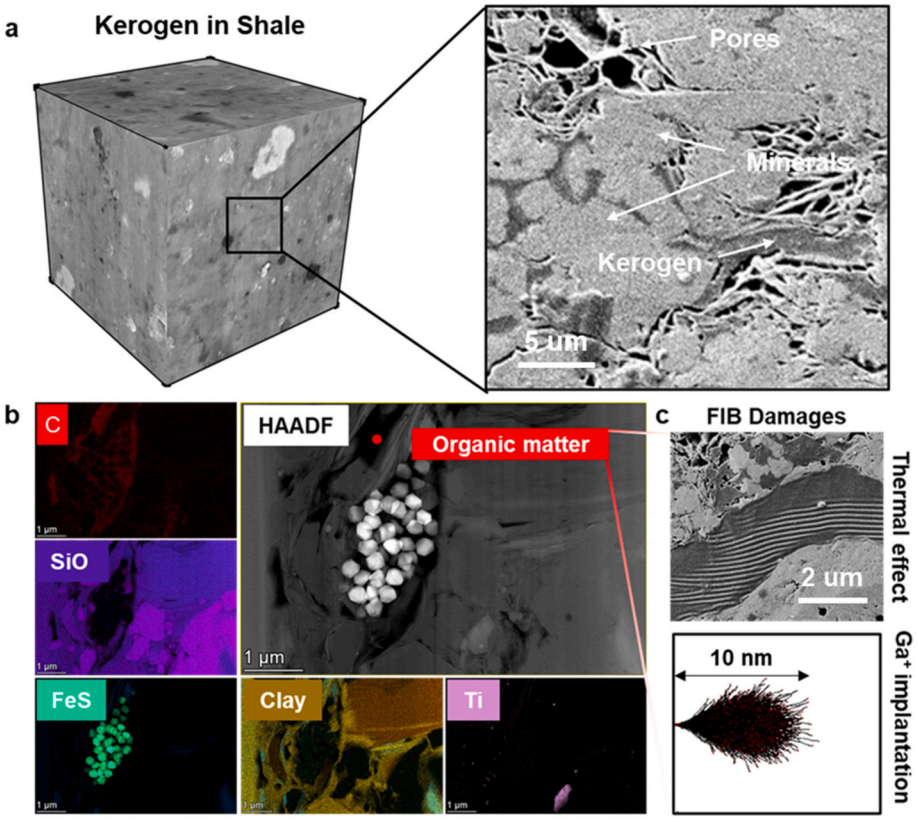

Fig. 1. Schematic of kerogen in shale and beam damage during FIB milling. (a) Schematic of a typical shale structure with inorganic and organic components and scanning electron microscope (SEM) image of a shale specimen. Different components are labeled. (b) High angle annular dark-field scanning transmission electron microscopy (HAADF) image of FIB lift-out shale specimen and the corresponding EDX mappings of different minerals and kerogen. While inorganic components preserve its crystallinity, the structure and chemistry of organic components are affected by two major FIB damage types: thermal stress and Ar^{+} or Ga^{+} ion implantation. (c) SEM image (top) reveal the damage due to thermal stress and SRIM simulation confirms the significant Ga^{+} implantation depth up to 20 nm using 30 keV accelerated voltage. Additional SEM images from the same sample are provided in Fig. S1.

2016; Liu et al., 2016) and UV–Visible absorption spectroscopy (Ferralis et al., 2015), more attention is required for advanced characterization methods (Josh et al., 2019) as well as specimen preparation for physical, mechanical and structural characterization.

As discussed above, the complex multiphases and composite nature of the source rock make it hard to isolate the ion milling damage. Here, the insoluble organic phase is first isolated from the source rock samples. The solid organic phase is referred throughout this study as kerogen, though other insoluble organics such as solid bitumen may also be present. The structure and composition of electron transparent kerogen specimen prepared by three techniques are characterized: low kV FIB, cryo-FIB, and cryomicrotome. Two major unavoidable damage mechanisms which are the thermal degradation due to the energetic impact of particles onto the material and the Ga^+ ion implantation effects during low kV FIB and cryo-FIB milling are observed. These damage mechanisms for kerogen are discussed based on different transmission electron microscopy (TEM) characterization techniques and the stopping range of ions in matter (SRIM) model. Interestingly, although the use of cryogenic temperature removes the thermal effect, Ga^+ ion implantation is observed in the specimen prepared by cryo-FIB. This observation challenges the common hypothesis that cryo-FIB techniques generally improve the quality of the organic specimen prepared through ion milling.

The magnitude of the thermal damage at a highly localized level was determined using nano-beam electron diffraction (NBED) performed at a low cryogenic temperature of −196 °C. Time-resolved diffraction patterns indicate that despite the fact kerogen is among the most stable geopolymers, the aromatic components still degraded due to the local temperature increases. On the other hand, the cryomicrotome technique has been extensively used in the biological sciences for electron microscopy investigation and is increasingly applied for example in X-ray and Raman microanalysis of biological and organic materials (Camp et al., 2014; Marshall, 2017). Herein the cryomicrotome technique operating at a temperature of −196 °C is demonstrated as a suitable method to prepare thin kerogen specimen while minimizing structural damage and preserving its native porosity and chemical composition.

2. Materials and methods

2.1. Specimen preparation

A late maturity source rock sample from a well that produced condensate with 4 wt% OM was crushed to form a powder, the soluble bitumen was extracted, and the rock matrix was digested to obtain the remaining insoluble OM. The solid organic phase is referred throughout this study as kerogen. The microscale OM grains selected for FIB preparation could not be characterized via Raman spectroscopy or other technique in order to distinguish between the different components that may be present. The density liquid separation method was used to obtain the float fraction of kerogen. The details of the kerogen isolation process and its characterization were previously described (Hull et al., 2019). This process generates kerogen powder, as seen in Fig. 2c, from which TEM foils were lifted. Thermal maturity parameters for the shale sample were determined by pyrolysis using a Rock-Eval instrument: S1 1.21 mg/g, S2 1.93 mg/g, S3 0.26 mg/g, production index 0.39, Tmax 452 °C, hydrogen index 50, oxygen index 7. The isolated kerogen was subjected to elemental analysis to obtain H/C 0.65, O/C 0.059, N/C 0.021.

2.2. Low keV FIB lift-out

Low keV FIB lift-out of kerogen specimen were first conducted using 30 keV accelerating voltage with beam current from 9 nA to 21 nA at ambient temperature for a thick lamella. The lamella with thickness of 2 μm was then mounted on the Cu grid using Pt deposition using 30 keV accelerating voltage with beam current 41 pA. Thinning of the lamella was conducted using a focused Ga^+ beam sequence at sequential accelerating voltages of 30, 16, and 5 keV, until the foil was electron transparent. The final milling was done at 5 keV, 64 pA Ga^+ ion beam. All the processes are performed in Thermo Fisher Scientific Helios G4 and schematically shown in Fig. 2.

2.3. Cryo-FIB lift-out

Cryo-FIB lift-out of kerogen specimen was conducted at liquid nitrogen temperature at −135 °C after using the conventional FIB lift-out of thick lamella with thickness of 3 μm. The thinning process is

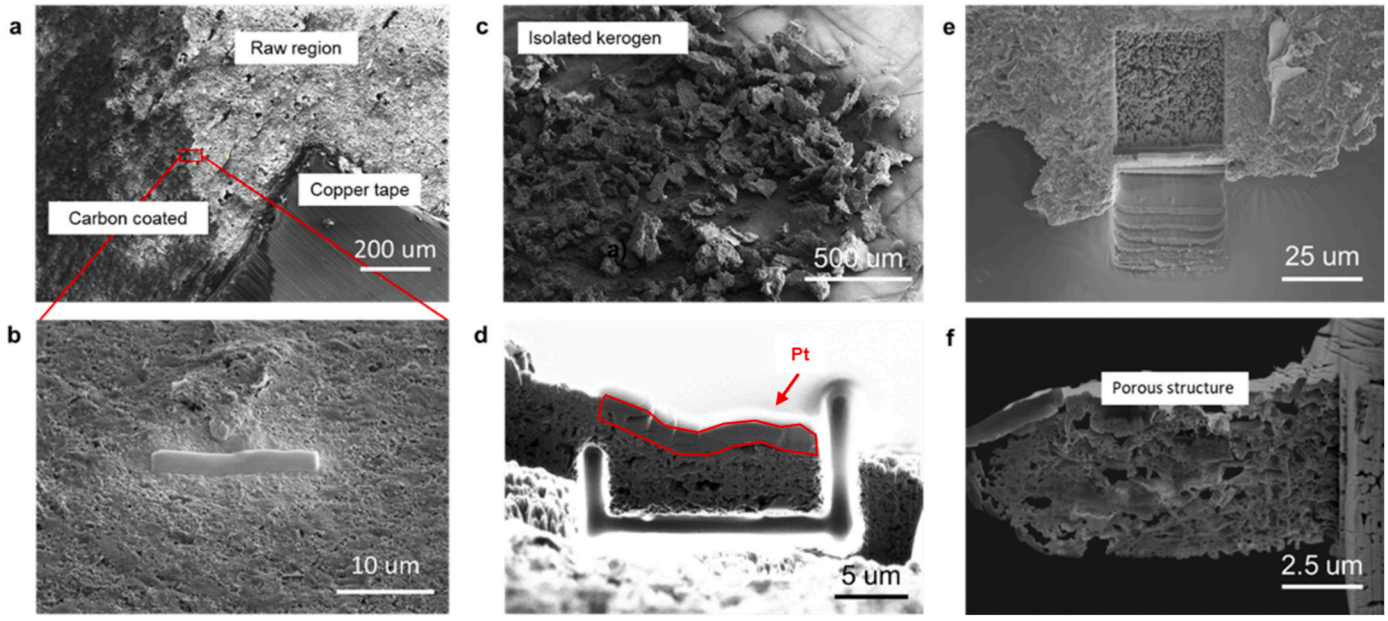

Fig. 2. Low-keV FIB lift-out technique. (a)–(b) SEM images show the overall morphology of the shale sample and the Pt protection on the region of interest. (c)–(f) SEM images demonstrate the lift-out process of isolated kerogen.

conducted using an accelerating voltage of 5 keV and 40 pA current to mill the thickness down to 60 nm at −135 °C. The cryo-FIB lift-out TEM specimens were then transferred from the FIB chamber to a side chamber which is maintained in a high vacuum (<5 × 10^{-6} Pa) at room temperature so that the specimens can be naturally warmed back to room temperature within 30 min.

2.4. Cryomicrotome

Kerogen powder was stabilized in 1% low-melting agarose, then cut into 0.5 mm cubes. Specimen were then infiltrated while rocking with 100% Epon resin with 4 exchanges over 8 h. The final polymerization was performed at room temperature over 7 days. Ultrathin sections (80 nm) were cut using a Leica FC6 Ultramicrotome (Leica, Wetzlar, Germany) with cryo-chamber attachment. The sectioning was performed at −80 °C with a Cryo 35 diamond knife (Diatome-US, Hatfield PA). A schematic of the process is shown in Fig. 3.

2.5. TEM characterization

The microstructure of TEM specimens prepared by either low keV FIB, cryo-FIB or cryomicrotome sectioned were analyzed using different TEM techniques. HAADF-STEM images and EDX elemental mapping and SAED pattern were collected using an aberration-corrected FEI ThemIS 80–300 operated at 300 kV with an Oxford Instruments X-Max 80 mm^2 EDX detector (Oxford Instruments, Abingdon, Oxfordshire, UK). NBED patterns are collected using FEI Titan operating at 300 keV either at room temperature or under cryogenic conditions. EELS was conducted using STEM aberration-corrected TEAM 1 operated with 300 keV accelerating voltage at room temperature. All the images processing was conducted using Gatan's Digital Micrograph software 4DSTEM (Savitzky et al., 2020).

2.6. Electron beam dose calculation

The time resolved NBED datasets were collected using a Gatan Orius charge coupled device on an FEI TitanX microscope at 300 kV operated in STEM mode with a small convergence semi-angle of α = 0.8 mrad and a camera length of 380 mm. The Gaussian-shaped probe size was measured to be 2.0 nm at full-width at half-maximum (FWHM) with beam current 12 pA. The dose or fluence (in $e^-/Å^2$) is estimated by calculating the average dose over the entire scanned area. Using the first method, a beam current of 12 pA with exposure of 50 ms covering the area of a circle of 10 nm (FWHM of probe) translates into an average dose of ~500 e^- $Å^{-2}$ for the nanobeam diffraction experiment in this work. According to the equation (2)), the local temperature reach ~250 °C during the imaging.

EELS experiments use a probe with 5 Å size at semi-convergence angle of 17 mrad with beam current of 15 pA. The dwell time is set to be 1s. The electron dose applied during acquisition of each spectrum was 2000 e^- $Å^{-2}$. The calculated local temperature is ~1000 °C.

2.7. Ion beam dose calculation

The Stopping Range of Ions in Matter (SRIM) code v. 2013 was used to compute the vacancies/angstrom/ion using a displacement energy of 30 keV (Agarwal et al., 2021). Considering the density of kerogen of 1.7 g/cm^3 and a beam current of 21 nA, the ion beam damage and Ga^+ content was calculated (Ward, 2010).

2.8. Nanoindentation

The powder of kerogen was mounted in epoxy resin. Diameter of specimens of approximate dimensions 3.5 cm were polished on SiC paper up to 4000 polishing grade, then polished again using a vibration polisher system to produce a smooth surface without a thin layer of polishing damage. The final polish abrasive size is 0.05 μm alumina polishing suspensions. Nanoindentation tests were conducted on a Bruker Ti 950 Triboindenter instrument at room temperature. A diamond Berkovich tip with a radius of around 250 nm was used with continuous stiffness measurement (CSM) method, which both hardness and elastic modulus as a function of indenter depth were measured at a time. The peak load was set to 6000 μN. All quantitative parameters were averaged over the 25 indentations with a spacing of 20 μm associated ±standard deviations.

3. Results

3.1. Microstructure characterization

As low dose bright-field TEM images show insufficient structural and compositional information (Supplementary Fig. S2), low dose HAADF-STEM was applied to investigate the microstructural and chemical composition of kerogen prepared by low kV FIB, cryo-FIB and cryomicrotome (Fig. 4a and detailed specimen preparation is in 2.2, 2.3, and 2.4). Thermal degradation was observed with wavy features (labeled with white arrow in HAADF-STEM image of low kV FIB in in Fig. 4a and Fig. S3), similar to the BIB milling in Fig. 1c, indicating that again the localized temperature during the ion milling, incidentally can exceed the melting or boiling temperature of the kerogen (Larsen et al., 2005). The enlargement of the pores in the kerogen sample suggests that the physical structure of the kerogen, in terms of pore size and pore

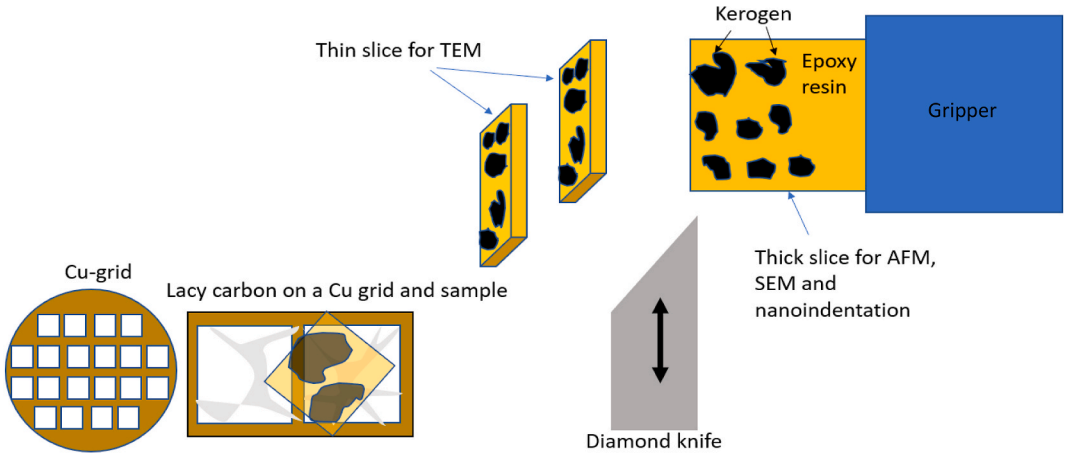

Fig. 3. Schematic of the cryo-microtome procedure for preparing kerogen samples.

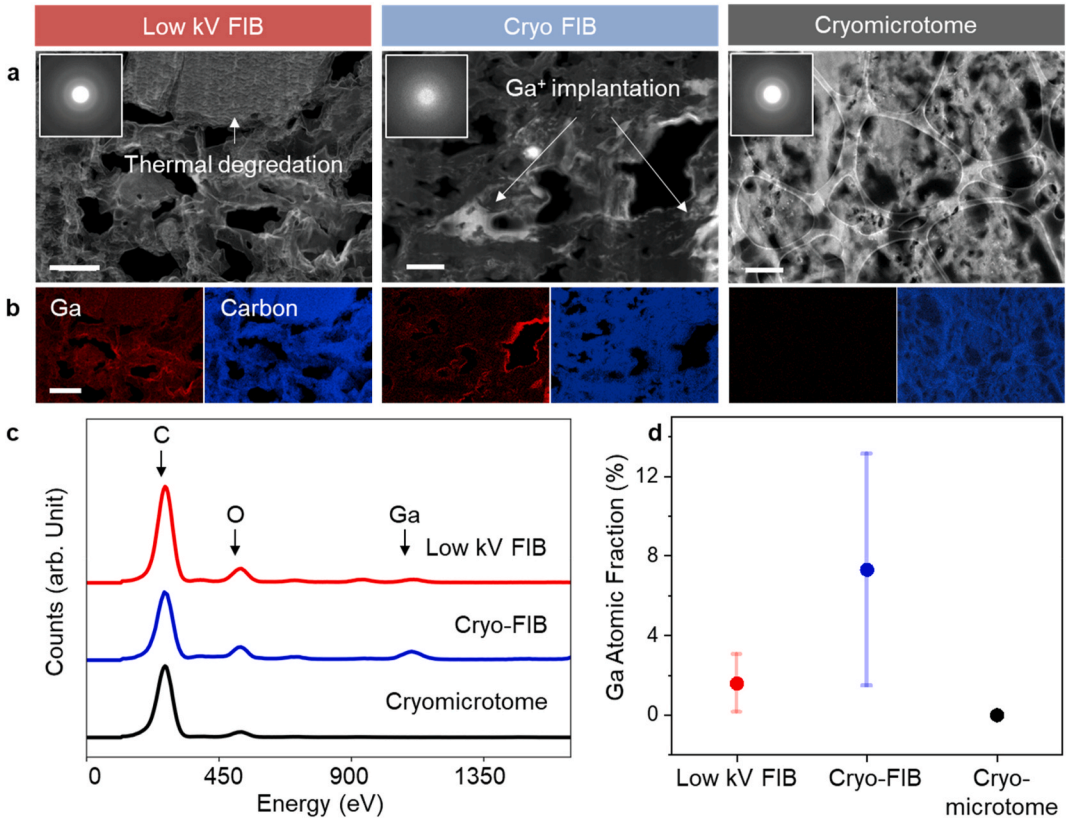

Fig. 4. TEM characterization. (a) HAADF images of specimen prepared by low kV FIB, cryo-FIB and cryomicrotome. The white arrows in the HAADF denote the damage region in each method. The inserts show the corresponding SAEDs with diffused rings due to the amorphous nature of the kerogen. (b) EDX mapping and representative diffraction pattern of kerogen in each method. The scale bars represent 1 μm in the HAADF and EDX mapping. (c) EDX spectrum of selected regions in three techniques. Major elements are labeled. (d) a plot of average Ga atomic fraction acquired from multiple EDX spectrums in three techniques shows the less Ga^+ contamination using low kV FIB. The error bars represent the standard deviation of the Ga atomic fraction.

connectivity, have also been changed during ion milling even using as low as 5 keV FIB (Supplementary Fig. S4). This structural damage to the kerogen polymeric matrix, affecting the pore sizes and their connecting polymer matrix and/or even disconnecting their structural in-situ organic matrix uniformity is misleading and give erroneous physical-imaging interpretations in the popular 3D-FIB reconstructing in FIB-SEM milling while estimating kerogen porosities and structures (Curtis et al., 2011; Hofmann et al., 2017; Loucks et al., 2009). HAADF imaging (Fig. 2b) of specimens prepared by cryo-FIB milling at a cryogenic temperature of −135 °C does not exhibit the wavy features, as observed on the kerogen macerals in Fig. 1 (c), once the thermal effect was minimized. However, distinct contrast and nonuniformity in the HAADF image were observed, particularly at the edges of the pores (labeled with white arrow in Fig. 4a, and also shown in the Supplementary Fig. S5). The contrast depends on the average atomic number (Z-contrast) in this mode of HAADF-STEM, suggesting that the bright region has undergone severe Ga^+ ion implantation incurred by the cryo-FIB milling. In kerogen specimen prepared by cryomicrotome, neither the wavy features nor contrast across the specimen is observed. The inset image in each HAADF image is the selected area electron diffraction (SAED) pattern obtained from the specimen prepared by three methods and confirm the amorphous nature of the kerogen. However, the diffraction pattern of the cryo-FIB specimen is more diffuse, which may be due to the severe Ga^+ ion implantation.

Energy dispersive x-ray (EDX) mapping at the three locations confirms the severe Ga^+ ion implantation, especially in the kerogen sample prepared by cryo-FIB milling. EDX mapping of gallium (Ga) and carbon (C) are shown in Fig. 4b. While C is uniform across the specimen, Ga^+ ions are clearly more concentrated near the edge of the pores. Fig. 4c are the EDX spectrum obtained from three specimen. The relatively higher Ga peak of the specimen prepared by cryo-FIB indicates more Ga^+ ion implantation that occurs during cryogenic milling. This conclusion is further supported by Fig. 4d, which shows the Ga atomic fraction calculated from multiple EDX mapping. Compared to the 1.7% Ga atomic fraction of low keV FIB prepared specimen, the higher Ga atomic fraction at around 7% of specimen prepared by cryo-FIB milling associated with the large standard deviation suggests the high non-uniformity of the implanted Ga^+ ions in the specimen and the possible severe accumulation of Ga^+ ions contamination. More careful studies are needed for kerogen preparations with different maturity i.e., chemical and porosities structures, to pin down the effects of the pore defects inflicted by Ga^+ ion implantation when using potential 3-D tomography techniques. The observations confirm that thermal effects and Ga^+ ion implantation are inevitable damage induced during conventional FIB and cryo-FIB milling, however, it can almost be entirely inhibited by cryomicrotome. These possible damage mechanisms are discussed in the following sections.

3.2. *Thermal effects in low kV FIB*

Focused ion beam (FIB) is known to induce thermal effects in soft OM including geological OM (Sanei and Ardakani, 2016). Initial attempts to quantify the residual effects of 30 keV Ga^+ ions on various types of geological OM demonstrated significant thermal alteration and suggest the potential for changes to the organic phase porosity particularly as a result of devolatilizing lighter compounds and implanting metal ions (Sanei and Ardakani, 2016). Fluorescence spectra obtained of milled specimen which sample a volume of the material exhibited minimal change, however, concluding that the thermal alteration was limited to within a few nm of the surface (Sanei and Ardakani, 2016). Other

studies, by contrast, showed no heating effects or damage to OM (Hackley et al., 2020). Sputtering shale surfaces with just 5 keV Ar^+ has been shown to alter the C1s spectra obtained using X-ray photoelectron spectroscopy (XPS) unless sputtering times are limited to less than 1 h (Cánneva et al., 2017). Both conventional BIB milling, and FIB milling can heat multiphase component specimens, with variable thermal conductivities to localized temperatures that will damage one phase or another (Hackley et al., 2020; Schmied et al., 2014). Unfortunately, this is the case for the deep source rock samples, as the localized temperature increases are far more pronounced in the OM, i.e., kerogen, bitumen, and others than that of the inorganic minerals due to its low thermal conductivities of 0.25–0.6 W $m^{-1}{\cdot}K^{-1}$, suggesting a higher degree of structural and chemical instability (Tarnawski et al., 2019). Thermal degradation of organic materials is known to result in the rearrangement and breaking of chemical bonds (Orthacker et al., 2014), warping of thin specimen due to thermal softening and changes in thermomechanical behavior (Hackley et al., 2020; Schmied et al., 2014). With a more converged ion beam down to 2 nm, the increase of local temperature induced by FIB on bulk specimen can be estimated by the following equation (Ishitani and Kaga, 1995):

$$\Delta T_{max} = \frac{0.75VI}{dk\pi} \quad (1)$$

where, V, is the accelerating voltage of the ion beam, I, the beam current, d, the beam diameter and k, the thermal conductivity of the specimen. The above equation does not include a term for radiative heat losses, however, and therefore can only be an estimation. In the protocol developed, final thinning of the specimen is finished with 5 keV accelerating voltage and 64 pA and the estimated local maximum temperature using equation (1) is over 300 °C, which is above the melting temperature of kerogen (Rajeshwar et al., 1980) and in agreement with the thermal effect and plastic flow observed in Fig. 4a. A recent study of patterning polymer thin films using conventional 30 keV FIB demonstrated that the modified region due to rapid temperature increase can extend beyond a depth of 15 nm, which suggests the thinning process of the kerogen specimen down to 100 nm may cause the enlargement of pores (Schmied et al., 2014) and indeed was observed in the low keV FIB specimen (Supplement Fig. S4). The thermal damage due to FIB may have been ignored in the previous electron microscopy studies of pore distribution and mechanical tests, in which 30 keV accelerating voltage is applied during the final thinning process (Curtis et al., 2011; Loucks et al., 2009).

To further support that the low keV milling process induces structural changes to the kerogen due to thermal effects, only the electron beam of the TEM was employed as a damage source to exclude the effects of Ga^+ ions contamination, from ion milling, while retaining the thermal effects and possible radiation damage. Graphitic domains with π–π stacking have been identified in the kerogen with electron diffraction methods (Delle Piane et al., 2018; Hou et al., 2019; Walters et al., 2014). These techniques have been underutilized for geological OM, though monitoring disruptions to these graphitic domains, developed during thermal carbonization (Brandes et al., 2008; Puech et al., 2019), could serve as a means to detect early signs of radiation damage to the kerogen (Hackley et al., 2021). NBED was performed at a cryogenic temperature of −196 °C to remove any thermal effect and at room temperature on the cryomicrotome-sectioned pure kerogen that had no prior ion beam damage. Fig. 5a and c display the representative time-resolved diffraction patterns that were collected with 300 keV accelerating voltage, 11 pA beam current electron beam that covered the area of a circle of 2 nm (FWHM of the probe). The increase of local temperature during NBED acquisition is calculated as 1200 °C, well above the temperature rise during low keV FIB milling. The characteristic diffraction spots correspond to the in-plane ~3.7 Å π–π spacing of the aromatic components of the kerogen (Panova et al., 2019). After starting data acquisition, the diffraction peaks in Fig. 5c started to diminish. This is consistent with the disappearance of π–π peaks at 2.7 $Å^{-1}$ in the corresponding radial intensity profile with an interval of 20 s in Fig. 5b. In comparison, performing the same experiment at −196 °C prevents the temperature rise caused by the electron beam but still produces radiation damage. The diffraction peaks in Fig. 5a remain intact even after 100 s, consistent with the radial intensity profiles in Fig. 5d. The clear differences indicate the loss of mass or crystallinity is attributed to the thermal effect caused by the electron beam but not the radiation effect.

The Kinchin-Pease model for electrons (relativistic) at 140 keV was used to estimate the threshold energy at which a displacement is created

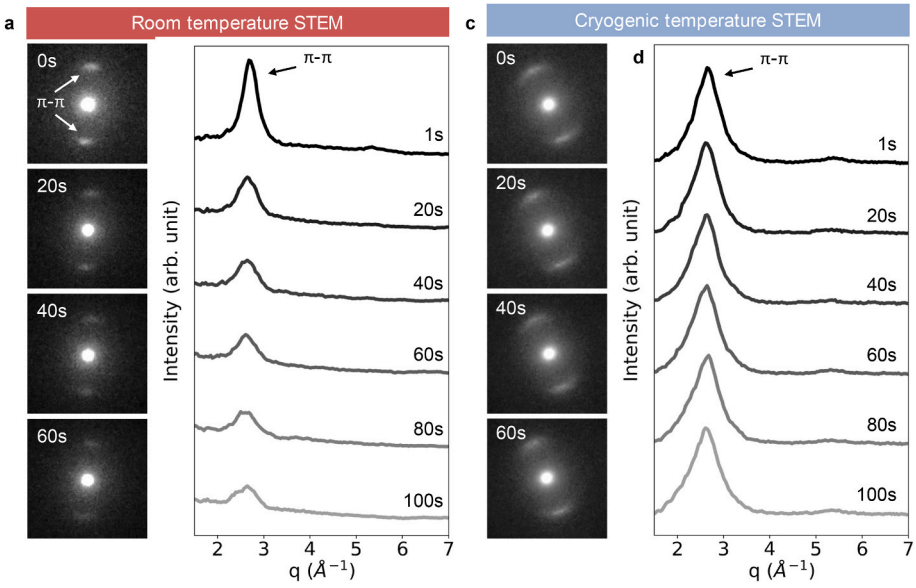

Fig. 5. Time resolved NBED results at room temperature TEM and cryogenic temperature TEM. (a) Time resolved NBED patterns obtained from the region with π-π stacking under the electron beam. Black arrow denotes the π-π peaks that fades as function of time. (b) Time-resolved radial intensity profiles that are corresponding to the NBED patterns. (c) Time resolved NBED patterns obtained from the region with π-π stacking under the electron beam using cryo-STEM technique. Black arrow denotes the π- π peaks that fades as function of time (d) Time-resolved radial intensity profiles obtained from NBED patterns that are corresponding to the NBED patterns using cryo-STEM technique.

using the equation below where E_{max} is the maximum energy transferred from the electron to cause a displacement and E_e is the acceleration energy, c is the speed of light, m_o is the mass of the electron and m_1 is the mass of the target (carbon) (Kinchin and Pease, 1955).

$$E_{max} = \frac{2}{m_1 c^2} E_e \left(E_e + 2 m_0 c^2\right)$$

Therefore, 300 keV is significantly above the threshold to cause radiation damage but can only cause two displacements in a head-on collision or one displacement on average. One can assume a displacement cross section for electrons on carbon at 300 keV of $\sigma_d = 13$ b leading to a total dose of 6.5×10^{-7} displacement per atoms (dpa) (Meyer et al., 2012). It is clear that the amount of elastic collision radiation damage is very limited which allows a valid assessment of the sample using TEM and supports the hypothesis that the structural changes of the kerogen are due to thermal effect. Therefore, the structural porosity changes are mostly due to the increase of the local temperature, evident in the sputtering action and the wavy topography of the kerogen macerals as shown in Fig. 1c. It is the thermal effect eventually that alters the molecular structure of the kerogen matrix instead of the radiation damage. Despite the fact that electrons with high accelerating voltage may induce chemical changes in kerogen, time-resolved electron energy loss spectroscopy (EELS) performed on pure kerogen in Fig. 6 does not show significant changes at the C K-edge and requires further study.

3.3. Ga^+ ion implantation in cryo-FIB

Recently developed Cryo-FIB equipped with a liquid nitrogen (LN_2) cooled stage at −135 °C has proved to be a suitable way to prepare thin organic materials for microscopic analysis such as the solid electrolyte interface (SEI) in Li-ion battery (Zachman et al., 2018) and soil for high resolution chemical analysis (Possinger et al., 2020). However, it is still unknown whether cryo-FIB milling can fully mitigate the ion beam milling damage (Vandenbroucke and Largeau, 2007) and previous chemical analysis of organic specimens after cryo-FIB milling have reported pronounced Ga^+ ion implantation that is consistent with the kerogen specimens shown in Fig. 1. The temperature-dependence of Ga^+ ion implantation on the specimen surface may be rationalized based on the following damage mechanism during the milling process of kerogen at cryogenic temperatures. First, the increased vapor pressure of Ga^+ ion compared to its bulk vapor pressure due to the Gibbs-Thomson effect in phase transition facilitates the accumulation of Ga^+ ions at the near surface (Fig. 7a). The red curve is calculated based on the Kelvin equation (Nachbar et al., 2018; Nanda et al., 2002), which corresponds to the vapor pressure increase over a surface of spherical nanoparticles assuming 187 pm, as the Ga^+ ion diameter:

$$p_{vapor}^{nano} = p_{vapor}^{bulk} \cdot e^{4 \cdot v \cdot \sigma / (k \cdot T \cdot d_{nano})} \quad (2)$$

Here, k is the Boltzmann constant, T is the temperature, ν is the molecular volume, d is the diameter of the particle and σ is the surface tension of the Ga^+ ion as function of temperature calculated by Hardy (Abbaschian, 1975). We also tracked the chamber pressure during the milling process of cryo-FIB and low kV FIB, as shown in Fig. 7b. The chamber pressure of cryo-FIB is one order of magnitude higher in cryo-FIB than that in low keV FIB indicating the Ga^+ ion is likely to accumulate at the near surface at a cryogenic temperature of −135 °C and sublimate during the low keV FIB milling at ambient temperatures with the local temperature rise above 80 °C due to ion beam heating. It is also reported that Ga^+ ion clusters can grow into larger particles during the warm up process (Dolph and Santeufemio, 2014). This explains the Ga^+ ion implantation around the edges of the pores and the large standard deviation of the Ga^+ ion distribution. In addition, the low temperature could slow down the Ga^+ ion out-diffusion from the specimen surface during milling. As the rate of diffusion decreases with temperature and particle size, cryogenic temperature inhibits atomic mobility and prevents out-diffusion of the Ga^+ ion implantation. It is known that at cryogenic temperature, hydrogen diffusivity is reported to be 8-12 orders of magnitude slower than at room temperature where it takes years to diffuse over 10 nm into heavier α-Ti (Chang et al., 2019). Hence, it is reasonable to expect slower out-diffusion of heavier implanted Ga atoms from the kerogen matrix at cryogenic temperatures. With all these considerations, it is reasonable to conclude that Ga^+ ion implantation is unavoidable or could even be more pronounced during cryo-FIB milling. The undesired Ga^+ ion implantation during specimen preparation not only makes precise structural assessment of kerogen specimens particularly challenging, but also hinders the microscopic physical-imaging investigation and the 3-D interpretation of structure-property relationships of the kerogen or any other OM present.

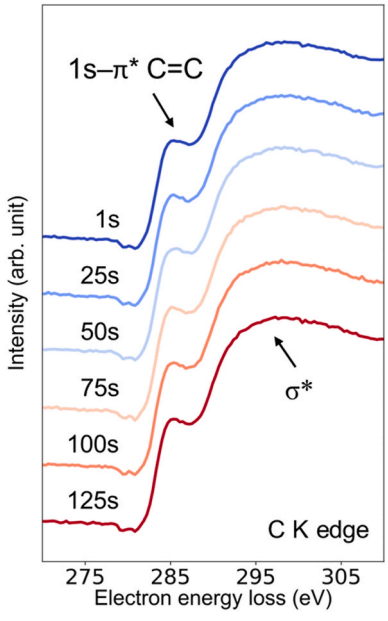

Fig. 6. Time-resolved EELS spectra at the C K-edge to determine the local chemical information of the kerogen under the electron beam with similar conditions.

3.4. Monte Carlo calculation of Ga^+ ion implantation

Significant Ga^+ ion implantation may alter the physical and chemical properties and structure of the kerogen (Bassim et al., 2012; Kim et al., 2011), and in particular, when 5 nm slices of source rocks are prepared by FIB-SEM and then tediously reconstructed to a 3-D volumetric representation of a source rock. A simple Monte Carlo simulation using stopping range of ions in matter 13 (SRIM-13) is performed to illustrate the intensity of the damage penetration depth and the interaction between Ga^+ ion and the kerogen organic phase in the shale sample. Fig. 8a shows the Ga^+ ion distribution and dpa (displacement per atom) as function of depth at the condition of 30 keV at 80° impact angle to the kerogen surface, which are equivalent to the typical milling conditions in these previous studies (Curtis et al., 2011, 2012; Saif et al., 2017) The calculations suggest that the implantation depth of Ga^+ ions can reach ~15–25 nm of the kerogen specimen associated with approximately 500 dpa while significant ion beam damages are created on the specimen surface during the ion milling. In contrast, Ga^+ ion beam with lower accelerating voltage could reduce the ion beam damage as expected. As shown in the distribution and displacement damage profile (Fig. 8a and b), the Ga^+ ion implantation depth decreases to less than ~6 nm associated with approximately 225 dpa. Although very low keV FIB techniques may reduce ion beam damage, the commonly used surface-sensitive measurements such as atomic force microscope (AFM) or nanoindentation may still be affected (Abedi et al., 2016; Li

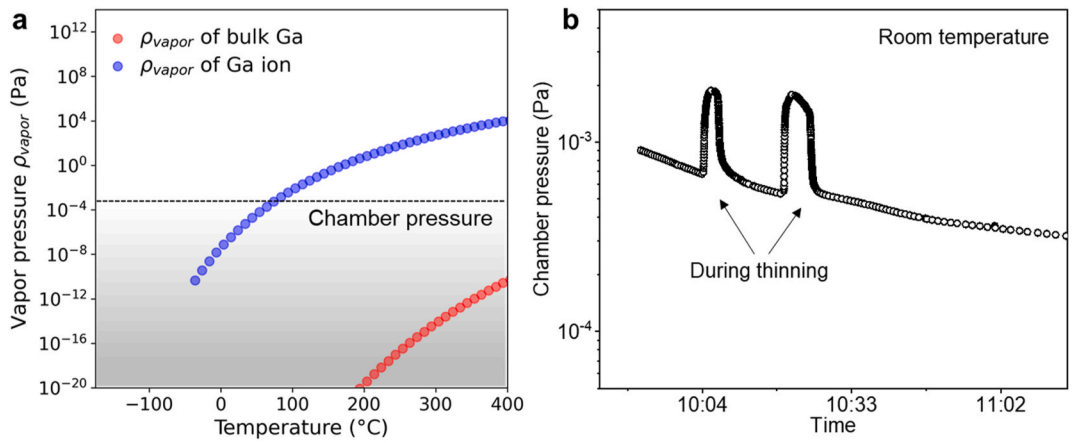

Fig. 7. Schematic of the increases of vapor pressure of Ga^+ due to Gibbs-Thomson effect and the measured chamber pressure of low kV FIB and cryo-FIB. (a) The decrease of the size of Ga^+ particle shift of the vapor pressure of Ga due to the Gibbs-Thomson effect. The dash line crosses the blue line at around 80 °C indicating there are high chances for Ga^+ to evaporate out from the kerogen surface during the milling. (b) The chamber pressure of the FIB used in this study confirming the pressure is around 10^{-3} Pa during the milling.

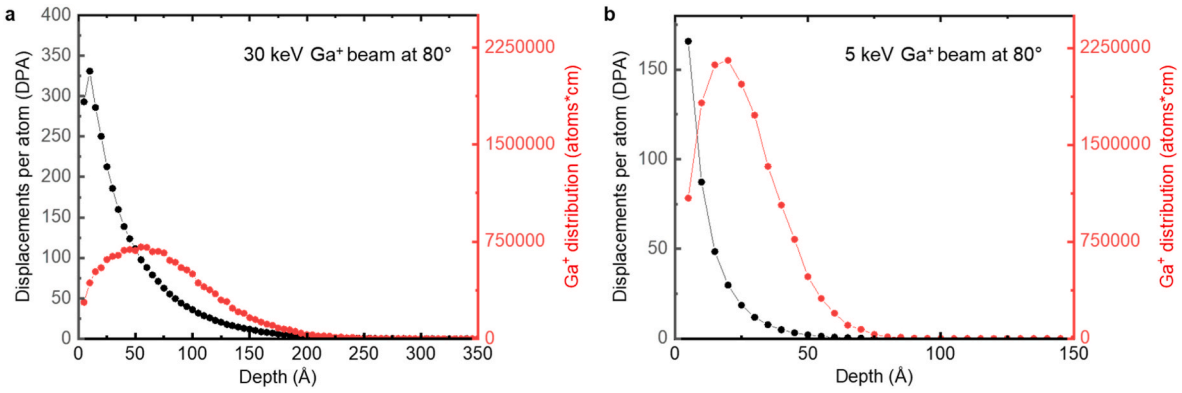

Fig. 8. SRIM calculation of Ga^+ ion beam damage in kerogen with density 1.7 g/cm^3. (a) Ga^+ distribution and displacements per atom as function of depth with 30 kV accelerated voltage at 80° impact angle. (b) Ga^+ ion distribution and displacements per atom as function of depth with 5 kV accelerated voltage at 80° impact angle.

et al., 2017; Yang et al., 2017) and Ga^+ implantation needs to be seriously considered for any quantitative analysis and/or property estimations (Wang et al., 2022).

3.5. Implications for microscopic kerogen interpretations

The process of isolating kerogen from source rock involves first extracting the soluble components (volatiles, bitumen, etc.) using organic solvent then aggressively demineralizing with HCl/HF to obtain a concentrated fraction of insoluble OM. This remaining kerogen (and pyrobitumen) is the most robust of the OM and thus any susceptibility to radiation damage can be expected to be more pronounced in the organic fractions than would exist in an intact source rock or source rock sample. Therefore, it is expected that the observed deterioration of the kerogen in the present study represents the best-case scenario for source rock OM under Ga^+ ion FIB beam radiation. As noted previously, the low thermal conductivity of the OM means that heat buildup in the organic domains is expected even in the presence of the mineral matrix as the minerals themselves will dissipate the heat more readily. Furthermore, the isolated kerogen used in the current study is late maturity gas window whereas lower maturity kerogen organic fractions are expected to be even more susceptible to FIB preparation damage.

Of relevance to drilling, completions, and stimulation operations in unconventional reservoirs is the mechanical properties of the source rock and how the *in situ* OM influences both compressive and tensile rock stresses under varying conditions. An initial look into the mechanical properties of isolated kerogen specimen prepared using cryomicrotome sectioning is provided in Supplementary Table 1. Nanoindentation of these samples demonstrates comparable hardness and Young's modulus values to that of conventional mechanically polished kerogen. These results are also in agreement with previous studies reporting that the hardness and the Young's Modulus are 0.9–1.3 GPa and 5–11 GPa (Ortega et al., 2007) indicating the diamond cutting from the microtome does not change the underlying structure.

For OM porosity estimations from source rock and shale microscopy, more work is needed to address the techniques available for preparing pristine source rock specimen for analysis (Iqbal et al., 2021). Cryomicrotome is observed to be a suitable technique for slicing pure kerogen for imaging or for mechanical properties study. However, attempts to study the physicochemical structure of kerogen pores will more likely require that the kerogen macerals remain unperturbed within the source rock matrix and with the bitumen and other polymeric components intact. Some studies have suggested that the organic pores are primarily hosted by the solid bitumen (Inan et al., 2018; Stokes et al., 2022). The implications for the current study are the same whether kerogen or solid bitumen, as the susceptibility to ion beam damage is dictated by their similar thermal conductivities. The damaging effects of low keV FIB demonstrated here or BIB demonstrated elsewhere (Sanei and Ardakani, 2016) point to the need to examine porosity and hence hydrocarbon storage and hydrocarbons reserve estimates when

examining the source rock porosity and its permeability structure through the lens of the electron microscope.

4. Conclusions

The microscopic investigation of the OM and kerogen within source-rock reservoirs is crucial for improved understanding of porosity and permeability within the reservoir hydrocarbons reserve estimates and the hydrofracking models, which have paramount economic and environmental importance. Further carbon dioxide sequestration (Hull and Abousleiman, 2021) considering source rock formations can also be impacted by the OM structure and its chemistry which require suitable microanalysis techniques to prepare damage-free electron transparent specimens for further microscopic investigation. In this study, the detailed mechanisms of the thermal effect and Ga^+ ion implantation that are typically observed in specimens prepared by low keV FIB and cryo-FIB are investigated. In contrast to the common hypothesis that cryo-FIB generally reduce the ion beam damage on the organic specimen preparation, the Ga^+ ion implantation from the cryo-FIB milling is explained by the decrease of vapor pressure at cryogenic temperature indicating the trade-off between the low-keV FIB and cryo-FIB. Cryo-microtome technique, alternatively, is shown to have potential as a suitable technique for preparing minimally damaged kerogen specimen. Overall, the discussion in this work could potentially extend to general organic materials, which attract increasing attention in recent years.

CRediT authorship contribution statement

Yujun Xie: Methodology, Investigation, Visualization, Writing – original draft. **Xi Huang:** Investigation. **Saleem Aldajani:** Investigation. **Hi T. Vo:** Investigation. **Danielle M. Jorgens:** Investigation. **Younane Abousleiman:** Conceptualization, Writing – review & editing. **Katherine Hull:** Writing – original draft, Writing – review & editing. **Peter Hosemann:** Supervision, Methodology, Writing – review & editing.

Declaration of competing interest

The authors declare that they have no known competing financial interests or personal relationships that could have appeared to influence the work reported in this paper.

Data availability

Data will be made available on request.

Acknowledgements

The TEM work was performed was performed at the National Center for Electron Microscopy, Molecular Foundry, Lawrence Berkeley National Laboratory. Cryo-FIB preparation was performed at the facility of Nanolab Technologies Inc.

Appendix A. Supplementary data

Supplementary data to this article can be found online at https://doi.org/10.1016/j.geoen.2023.212607.

References

Abbaschian, G., 1975. Surface tension of liquid gallium. Journal of the Less Common Metals 40, 329–333.
Abedi, S., Slim, M., Hofmann, R., Bryndzia, T., Ulm, F.-J., 2016. Nanochemo-mechanical signature of organic-rich shales: a coupled indentation–EDX analysis. Acta Geotechnica 11, 559–572.
Abousleiman, Y.N., Hull, K.L., Han, Y., Al-Muntasheri, G., Hosemann, P., Parker, S., Howard, C.B., 2016. The granular and polymer composite nature of kerogen-rich shale. Acta Geotechnica 11, 573–594.
Agarwal, S., Lin, Y., Li, C., Stoller, R.E., Zinkle, S.J., 2021. On the use of SRIM for calculating vacancy production: Quick calculation and full-cascade options. Nucl. Instrum. Methods Phys. Res. Sect. B Beam Interact. Mater. Atoms 503, 11–29.
Babu, R.P., Irukuvarghula, S., Harte, A., Preuss, M., 2016. Nature of gallium focused ion beam induced phase transformation in 316L austenitic stainless steel. Acta Mater. 120, 391–402.
Bassim, N.D., DE Gregorio, B.T., Kilcoyne, A.L.D., Scott, K., Chou, T., Wirick, S., Cody, G., Stroud, R.M., 2012. Minimizing damage during FIB sample preparation of soft materials. J. Microsc. 245, 288–301.
Bennett, K.C., Berla, L.A., Nix, W.D., Borja, R.I., 2015. Instrumented nanoindentation and 3D mechanistic modeling of a shale at multiple scales. Acta Geotechnica 10, 1–14.
Brandes, J.A., Cody, G.D., Rumble, D., Haberstroh, P., Wirick, S., Gelinas, Y., 2008. Carbon K-edge XANES spectromicroscopy of natural graphite. Carbon 46, 1424–1434.
Camp Jr., C.H., Lee, Y.J., Heddleston, J.M., Hartshorn, C.M., Walker, A.R.H., Rich, J.N., Lathia, J.D., Cicerone, M.T., 2014. High-speed coherent Raman fingerprint imaging of biological tissues. Nat. Photonics 8, 627–634.
Cánneva, A., Giordana, I.n.S., Erra, G., Calvo, A., 2017. Organic matter characterization of shale rock by X-ray photoelectron spectroscopy: adventitious carbon contamination and radiation damage. Energy Fuels 31, 10414–10419.
Chang, Y., Lu, W., Guénolé, J., Stephenson, L.T., Szczpaniak, A., Kontis, P., Ackerman, A. K., Dear, F.F., Mouton, I., Zhong, X., 2019. Ti and its alloys as examples of cryogenic focused ion beam milling of environmentally-sensitive materials. Nat. Commun. 10, 1–10.
Curtis, M.E., Ambrose, R.J., Sondergeld, C.H., Rai, C.S., 2011. Investigation of the Relationship between Organic Porosity and Thermal Maturity in the Marcellus Shale. North American Unconventional Gas Conference and Exhibition.
Curtis, M.E., Cardott, B.J., Sondergeld, C.H., Rai, C.S., 2012. Development of organic porosity in the Woodford Shale with increasing thermal maturity. Int. J. Coal Geol. 103, 26–31.
Delle Piane, C., Bourdet, J., Josh, M., Clennell, M.B., Rickard, W.D., Saunders, M., Sherwood, N., Li, Z., Dewhurst, D.N., Raven, M.D., 2018. Organic matter network in post-mature Marcellus Shale: effects on petrophysical properties. AAPG (Am. Assoc. Pet. Geol.) Bull. 102, 2305–2332.
Dolph, M.C., Santeufemio, C., 2014. Exploring cryogenic focused ion beam milling as a Group III–V device fabrication tool. Nucl. Instrum. Methods Phys. Res. Sect. B Beam Interact. Mater. Atoms 328, 33–41.
Ferralis, N., Liu, Y., Bake, K.D., Pomerantz, A.E., Grossman, J.C., 2015. Direct correlation between aromatization of carbon-rich organic matter and its visible electronic absorption edge. Carbon 88, 139–147.
Ferralis, N., Matys, E.D., Knoll, A.H., Hallmann, C., Summons, R.E., 2016. Rapid, direct and non-destructive assessment of fossil organic matter via microRaman spectroscopy. Carbon 108, 440–449.
Grobe, A., Schmatz, J., Littke, R., Klaver, J., Urai, J.L., 2017. Enhanced surface flatness of vitrinite particles by broad ion beam polishing and implications for reflectance measurements. Int. J. Coal Geol. 180, 113–121.
Hackley, P.C., Jubb, A.M., McAleer, R.J., Valentine, B.J., Birdwell, J.E., 2021. A review of spatially resolved techniques and applications of organic petrography in shale petroleum systems. Int. J. Coal Geol., 103745
Hackley, P.C., Jubb, A.M., Valentine, B.J., Hatcherian, J.J., Yu, J.-J., Podrazky, W.K., 2020. Investigating the effects of broad ion beam milling to sedimentary organic matter: surface flattening or heat-induced aromatization and condensation? Fuel 282, 118627.
Hofmann, F., Tarleton, E., Harder, R.J., Phillips, N.W., Ma, P.W., Clark, J.N., Robinson, I. K., Abbey, B., Liu, W., Beck, C.E., 2017. nan et alSci Rep 7, 45993.
Hou, Y., Zhang, K., Wang, F., He, S., Dong, T., Wang, C., Qin, W., Xiao, Y., Tang, B., Yu, R., 2019. Structural evolution of organic matter and implications for graphitization in over-mature marine shales, south China. Mar. Petrol. Geol. 109, 304–316.
Hull, K.L., Abousleiman, Y.N., 2016. Insights on the REV of source shale from nano- and micromechanics. In: Jin, C., Cusatis, G. (Eds.), New Frontiers in Oil and Gas Exploration. Springer International Publishing, Cham, pp. 335–366.
Hull, K.L., Abousleiman, Y.N., 2021. Chemomechanical effects of oxidizer-CO2 systems upon hydraulically fractured unconventional source rock. Can. J. Chem. Eng.
Hull, K.L., Abousleiman, Y.N., Han, Y., Al-Muntasheri, G.A., Hosemann, P., Parker, S.S., Howard, C.B., 2017. Nanomechanical characterization of the tensile modulus of rupture for kerogen-rich shale. SPE J. 22, 1024–1033.
Hull, K.L., Jacobi, D., Abousleiman, Y.N., 2019. Oxidative kerogen degradation: a potential approach to hydraulic fracturing in unconventionals. Energy Fuels 33, 4758–4766.
Inan, S., Al Badairy, H., İnan, T., Al Zahrani, A., 2018. Formation and occurrence of organic matter-hosted porosity in shales. Int. J. Coal Geol. 199, 39–51.
Inan, S., Hakami, A., AbuAli, M.A., 2017. A petroleum system and basin modeling study of Northwest and East-Central Saudi Arabia: effect of burial history and adjacent rock lithology on the gas potential of the Silurian Qusaiba shales. In: AbuAli, M.A., Moretti, I., Nordgard, H.M. (Eds.), Petroleum Systems Analysis-Case Studies. AAPG Memoir, p. 35.
Iqbal, O., Padmanabhan, E., Mandal, A., Dvorkin, J., 2021. Characterization of geochemical properties and factors controlling the pore structure development of shale gas reservoirs. J. Petrol. Sci. Eng. 206, 109001.
Ishitani, T., Kaga, H., 1995. Calculation of local temperature rise in focused-ion-beam sample preparation. Microscopy 44, 331–336.
Josh, M., Delle Piane, C., Esteban, L., Bourdet, J., Mayo, S., Pejcic, B., Burgar, I., Luzin, V., Clennell, M.B., Dewhurst, D.N., 2019. Advanced laboratory techniques characterising solids, fluids and pores in shales. J. Petrol. Sci. Eng. 180, 932–949.

Josh, M., Esteban, L., Delle Piane, C., Sarout, J., Dewhurst, D.N., Clennell, M.B., 2012. Laboratory characterisation of shale properties. J. Petrol. Sci. Eng. 88–89, 107–124.
Katz, B.J., Arango, I., 2018. Organic porosity: a geochemist's view of the current state of understanding. Org. Geochem. 123, 1–16.
Kiener, D., Motz, C., Rester, M., Jenko, M., Dehm, G., 2007. FIB damage of Cu and possible consequences for miniaturized mechanical tests. Mater. Sci. Eng., A 459, 262–272.
Kim, S., Jeong Park, M., Balsara, N.P., Liu, G., Minor, A.M., 2011. Minimization of focused ion beam damage in nanostructured polymer thin films. Ultramicroscopy 111, 191–199.
Kinchin, G.H., Pease, R.S., 1955. The displacement of atoms in solids by radiation. Rep. Prog. Phys. 18, 1.
Larsen, J.W., Islas-Flores, C., Aida, M.T., Opaprakasit, P., Painter, P., 2005. Kerogen chemistry 2. Low-temperature anhydride formation in kerogens. Energy Fuels 19, 145–151.
Li, C., Ostadhassan, M., Kong, L., 2017. Nanochemo-mechanical characterization of organic shale through AFM and EDS. In: SEG Technical Program Expanded Abstracts 2017. Society of Exploration Geophysicists, pp. 3837–3840.
Liu, Y., Ferralis, N., Bryndzia, L.T., Grossman, J.C., 2016. Genome-inspired molecular identification in organic matter via Raman spectroscopy. Carbon 101, 361–367.
Loucks, R.G., Reed, R.M., Ruppel, S.C., Jarvie, D.M., 2009. Morphology, genesis, and distribution of nanometer-scale pores in siliceous mudstones of the Mississippian Barnett Shale. J. Sediment. Res. 79, 848–861.
Marshall, A.T., 2017. Quantitative x-ray microanalysis of model biological samples in the SEM using remote standards and the XPP analytical model. J. Microsc. 266, 231–238.
Maxwell, S., 2011. Microseismic hydraulic fracture imaging: the path toward optimizing shale gas production. Lead. Edge 30, 340–346.
Mayer, J., Giannuzzi, L.A., Kamino, T., Michael, J., 2007. TEM sample preparation and FIB-induced damage. MRS Bull. 32, 400–407.
Meyer, J.C., Eder, F., Kurasch, S., Skakalova, V., Kotakoski, J., Park, H.J., Roth, S., Chuvilin, A., Eyhusen, S., Benner, G., 2012. Accurate measurement of electron beam induced displacement cross sections for single-layer graphene. Phys. Rev. Lett. 108, 196102.
Milner, M., McLin, R., Petriello, J., 2010. Imaging texture and porosity in mudstones and shales: comparison of secondary and ion-milled backscatter SEM methods, Canadian unconventional resources and international petroleum conference. OnePetro.
Nachbar, M., Duft, D., Leisner, T., 2018. The vapor pressure over nano-crystalline ice. Atmos. Chem. Phys. 18, 3419–3431.
Nanda, K., Kruis, F., Fissan, H., 2002. Evaporation of free PbS nanoparticles: evidence of the Kelvin effect. Phys. Rev. Lett. 89, 256103.
Ortega, J.A., Ulm, F.-J., Abousleiman, Y., 2007. The effect of the nanogranular nature of shale on their poroelastic behavior. Acta Geotechnica 2, 155–182.
Orthacker, A., Schmied, R., Chernev, B., Fröch, J., Winkler, R., Hobisch, J., Trimmel, G., Plank, H., 2014. Chemical degradation and morphological instabilities during focused ion beam prototyping of polymers. Phys. Chem. Chem. Phys. 16, 1658–1666.
Panova, O., Ophus, C., Takacs, C.J., Bustillo, K.C., Balhorn, L., Salleo, A., Balsara, N., Minor, A.M., 2019. Diffraction imaging of nanocrystalline structures in organic semiconductor molecular thin films. Nat. Mater. 18, 860–865.
Possinger, A.R., Zachman, M.J., Enders, A., Levin, B.D., Muller, D.A., Kourkoutis, L.F., Lehmann, J., 2020. Organo–organic and organo–mineral interfaces in soil at the nanometer scale. Nat. Commun. 11, 1–11.
Puech, P., Dabrowska, A., Ratel-Ramond, N., Vignoles, G.L., Monthioux, M., 2019. New insight on carbonisation and graphitisation mechanisms as obtained from a bottom-up analytical approach of X-ray diffraction patterns. Carbon 147, 602–611.
Rajeshwar, K., DuBow, J.B., Rosenvold, R.J., 1980. Dependence of thermal conductivity on organic content for green river oil shales. Ind. Eng. Chem. Prod. Res. Dev. 19, 629–632.
Saif, T., Lin, Q., Butcher, A.R., Bijeljic, B., Blunt, M.J., 2017. Multi-scale multi-dimensional microstructure imaging of oil shale pyrolysis using X-ray micro-tomography, automated ultra-high resolution SEM, MAPS Mineralogy and FIB-SEM. Appl. Energy 202, 628–647.
Sanei, H., 2020. Genesis of solid bitumen. Sci. Rep. 10, 15595.
Sanei, H., Ardakani, O.H., 2016. Alteration of organic matter by ion milling. Int. J. Coal Geol. 163, 123–131.
Savitzky, B.H., Hughes, L.A., Zeltmann, S.E., Brown, H.G., Zhao, S., Pelz, P.M., Barnard, E.S., Donohue, J., DaCosta, L.R., Pekin, T.C., 2020. py4DSTEM: A Software Package for Multimodal Analysis of Four-Dimensional Scanning Transmission Electron Microscopy Datasets arXiv preprint arXiv:2003.09523.
Schmied, R., Fröch, J.E., Orthacker, A., Hobisch, J., Trimmel, G., Plank, H., 2014. A combined approach to predict spatial temperature evolution and its consequences during FIB processing of soft matter. Phys. Chem. Chem. Phys. 16, 6153–6158.
Stokes, M.R., Valentine, B.J., Hackley, P.C., Jubb, A.M., 2022. Relating systematic compositional variability to the textural occurrence of solid bitumen in shales. Int. J. Coal Geol. 261, 104068.
Tarnawski, V.R., Tsuchiya, F., Coppa, P., Bovesecchi, G., 2019. Volcanic soils: inverse modeling of thermal conductivity data. Int. J. Thermophys. 40, 14.
Turcotte, D.L., Moores, E.M., Rundle, J.B., 2014. Super fracking. Phys. Today 67, 34–39.
Ulm, F.-J., Abousleiman, Y., 2006. The nanogranular nature of shale. Acta Geotechnica 1, 77–88.
Valentine, B.J., Hackley, P.C., Hatcherian, J., Yu, J.-J., 2019. Reflectance increase from broad beam ion milling of coals and organic-rich shales due to increased surface flatness. Int. J. Coal Geol. 201, 86–101.
Vandenbroucke, M., Largeau, C., 2007. Kerogen origin, evolution and structure. Org. Geochem. 38, 719–833.
Volkert, C.A., Minor, A.M., 2007. Focused ion beam microscopy and micromachining. MRS Bull. 32, 389–399.
Walters, C.C., Kliewer, C.E., Awwiller, D.N., Rudnicki, M.D., Passey, Q.R., Lin, M.W., 2014. Influence of turbostratic carbon nanostructures on electrical conductivity in shales. Int. J. Coal Geol. 122, 105–109.
Wang, T., Wang, Q., Zhang, P., Cheng, S., Anyimah, P.O., Tan, Y., Tian, S., 2022. Application of atom force microscope and nanoindentation to characterize nanoscale mechanical properties of shale before and after supercritical CO2 immersion. J. Petrol. Sci. Eng. 212, 110348.
Ward, J.A., 2010. Kerogen density in the marcellus shale. SPE Unconventional Gas Conference.
Yang, J., Hatcherian, J., Hackley, P.C., Pomerantz, A.E., 2017. Nanoscale geochemical and geomechanical characterization of organic matter in shale. Nat. Commun. 8, 1–9.
Zachman, M.J., Tu, Z., Choudhury, S., Archer, L.A., Kourkoutis, L.F., 2018. Cryo-STEM mapping of solid–liquid interfaces and dendrites in lithium-metal batteries. Nature 560, 345–349.
Zeszotarski, J.C., Chromik, R.R., Vinci, R.P., Messmer, M.C., Michels, R., Larsen, J.W., 2004. Imaging and mechanical property measurements of kerogen via nanoindentation. Geochem. Cosmochim. Acta 68, 4113–4119.
Zhao, J., Zhang, D., 2020. Dynamic microscale crack propagation in shale. Eng. Fract. Mech. 228.